Int J Adv Manuf Technol (2017) 93:4305–4316
DOI 10.1007/s00170-017-0844-6

ORIGINAL ARTICLE

The influence of energy distribution factor during laser-MIG hybrid welding of Invar alloy

Xiaohong Zhan[1,2] · **Cailin Zhang**[1] · **Yun Liu**[1] · **Ling Xia**[1]

Received: 9 March 2017 / Accepted: 18 July 2017 / Published online: 5 August 2017

Abstract In this study, a three-dimensional (3D) finite element model was established to predict the shape of the molten zone and the temperature fields of multi-layer laser–MIG hybrid welding for Fe36Ni Invar alloy. The multi-layer laser–MIG hybrid welding experiments of 19.05-mm-thick Invar plates were conducted to obtain the well-welded joints. The molten zone shapes were compared to the simulated results to figure out the relation between the energy distribution factor and the welding temperature field. A combined heat source model was proposed to describe the interaction between laser heat source and arc heat source. Besides, the empirical formula of energy distribution factor was given. The metallography detection results showed that the increasing ratio of laser power in hybrid welding could increase the weld penetration depth and the increasing ratio of arc power in hybrid welding could increase the weld width. In addition, it was also found that the laser heat source in hybrid welding heat source contributed equiaxed grains, and weld centerlines had rotation, due to different ratios of energy distribution during the multi-layer laser–MIG hybrid welding.

Keywords Laser–MIG hybrid welding · Combined heat source model · Invar alloy · Ratio of energy distribution

✉ Xiaohong Zhan
xiaohongzhan_nuaa@126.com

[1] College of Material Science and Technology, Nanjing University of Aeronautics and Astronautics, Nanjing 211106, China

[2] Department of Materials Science and Engineering, The Ohio State University, Columbus, OH 43210, USA

Abbreviations

LIP	Laser-induced plasma
FZ	Fusion zone
BM	Base metal

1 Introduction

Invar alloy has been widely used to manufacture the molds of composite material structures for aerospace and precise instruments, due to its very low coefficient of thermal expansion comparing to other metals such as ordinary carbon steel and aluminum alloy [1]. Also, because of the low thermal expansion coefficient, invar alloy has a good corrosion resistance and good toughness. However, aircraft composite components are so large and complex that one-step modeling is difficult for mold manufacturing. Thus, welding becomes one of the most important methods for mold manufacturing [2]. The bulk of the literature is specifically dedicated to Invar cites as the main problem with welding is its acute sensitivity to reheat cracking [3]. Consequently, it makes welding of invar36 alloy become a challenge.

With traditional single heat source welding method, it is hard to acquire good weldment of Invar alloy. By combining laser welding and arc welding, the advantages of the hybrid welding technique compared to pure laser welding or arc welding are well known and include an increase in the welding speed, the weldable material thickness, the gap bridging ability, and the welding process stability and efficiency. At present, there are many attempts to use laser–arc hybrid welding [4–6]. During the laser–arc welding, the temperature field inside welded joint greatly influences stress distributions, deformation, and grain growth [7, 8]. Whereas the numerical modeling of temperature field has an extremely accurate description of heat transfer that occurs in the weld pool, it depends on the determining heat

sources [9, 10]. Consequently, the numerical model is used to predict the geometrical characteristic of the fusion zone and calculate the temperature field in this work [11–14].

At present, worldwide, to improve the heat source model for laser–MIG hybrid welding, many researchers have made much more effort and attempts. Xu et al. [15] proposed four new kinds of distribution functions of volumetric heat sources according to the geometry and dimension of weld cross sections in laser + GMAW welding, upon which the adaptive combined volumetric heat source modes for hybrid welding were developed. It was found that the predicted weld penetration depth, width, and fusion line locus all agree well with the experimental results. Chen et al. [16] experimentally studied the hybrid laser–arc welding of stainless steel and observed the interaction between the laser beam and arc plasma. In laser welding alone and hybrid laser/arc welding of high-strength aluminum alloys, a large number of transverse cracks are also found in the weld fusion zone, as reported by Hu and Richardson [17]. Kong et al. [18] performed a series of experiments to verify the developed thermo-mechanical finite element model (FEM), and a qualitative agreement of residual stress distribution and weld geometrical size is shown to exist. Zhan et al. [19] established a plane–conical combined heat source model to simulate the laser–MIG hybrid welding process. The effect of welding layer for Invar36 alloy on the temperature field, residual stress, and deformation distribution was studied. It was investigated that the maximum residual stress of Invar plates is 300 MPa and the maximum deformation is 0.4 mm. Lyes et al. [20] predicted the shape of the molten zone and the temperature field inside parts on the basis of experimental design and numerical modeling establishment. In modeling of laser–MIG hybrid welding, energy distribution factor of the combined heat source for laser–MIG hybrid welding determines the temperature field and microstructure because of the interaction between laser heat source and arc heat source [5, 21–23]. Furthermore, there are few studies about energy distribution factor of the combined heat source for laser–arc hybrid welding [24].

In this paper, multi-layer laser–MIG hybrid welding experiments were conducted for the 19.5-mm-thick Invar plates. In particular, the empirical formula of energy distribution factor of the combined heat source for laser–MIG hybrid welding was produced on the basis of interaction mechanism between laser and arc in laser–MIG hybrid welding. The validation of energy distribution factor of the combined heat source proposed was carried out by comparing the numerical simulation with experimental results. Finally, the morphology and microstructure of the butt joint were investigated and discussed.

2 Experimental design

The multi-layer laser–MIG hybrid welding experiments are carried out, employing an IPG YLS-6000 laser device with a maximum power output available equal to 6 kW, which couples with a TPS-5000 FRONIUS welding machine, as shown in Table 2. The laser source is delivered via a 200-μm-diameter fiber, with a beam parameter product (BPP) equal to 4.0 mm per mrad. The laser beam, whose wavelength is 1.07 μm, is focused by a lens with a focal distance equal to 250 mm producing a spot diameter of 0.4 mm on the surface of the workpieces. The TPS-5000 FRONIUS welding machine provides arc heat source and is attached to a Kuka (KR30H) welding robot to capacitate simultaneous moving (Fig. 1).

The dimensions of Invar alloy sample are 50 × 50× 19.05 mm^3, of which the chemical composition is listed in Table 1. For Invar base metal alloy, the filler wire must have nearly the same chemical composition and mechanical properties must be a bit greater in order to avoid problems during and after welding to compensate the deterioration of mechanical properties after welding. Therefore, an Invar M93 filler wire is used, whose chemical composition is shown in Table 1. Before the experiment, the Invar plates are machined to be v-groove with a 30° beveling angle and 5-mm root face, as shown in Fig. 2. The workpieces are polished with sandpaper and wiped with acetone and alcohol to avoid the debris and greasy dirt remaining on the surface. To ensure arc stability and weld penetration depth and reduce the spatter, the gas mixture of 20% CO_2 and 80% Ar is used as shielding gas. Through a lot of the laser–MIG hybrid welding experiments, three groups of good-formed welded joint are obtained in optimal welding parameters including laser power, welding speed, current, and voltage shown in Tables 2 3.

3 Modeling

3.1 Meshing

Hexahedral elements are chosen to mesh geometric considering the calculation of accuracy, velocity, and convergence. The geometric model is meshed into 150,826 solid elements and 158,041 nodes, of which the minimum mesh size is 0.5 × 0.5 × 0.5 mm^3, and the maximum mesh size is 2 × 3 × 4.5 mm^3. In order to improve computational efficiency, the meshes in welded seam are fine and the meshes in base metal zone are relatively coarse.

3.2 Heat transfer equation and boundary conditions

For analysis of three-dimensional heat transfer mathematical model, the governing equation based on energy conservation can be specialized into a differential control volume which is shown as follows [25]:

$$\frac{\partial}{\partial x_i}\left(\lambda_{ij}\frac{\partial T}{\partial x_j}\right)+Q-\rho c\frac{\partial T}{\partial t}=0 \tag{1}$$

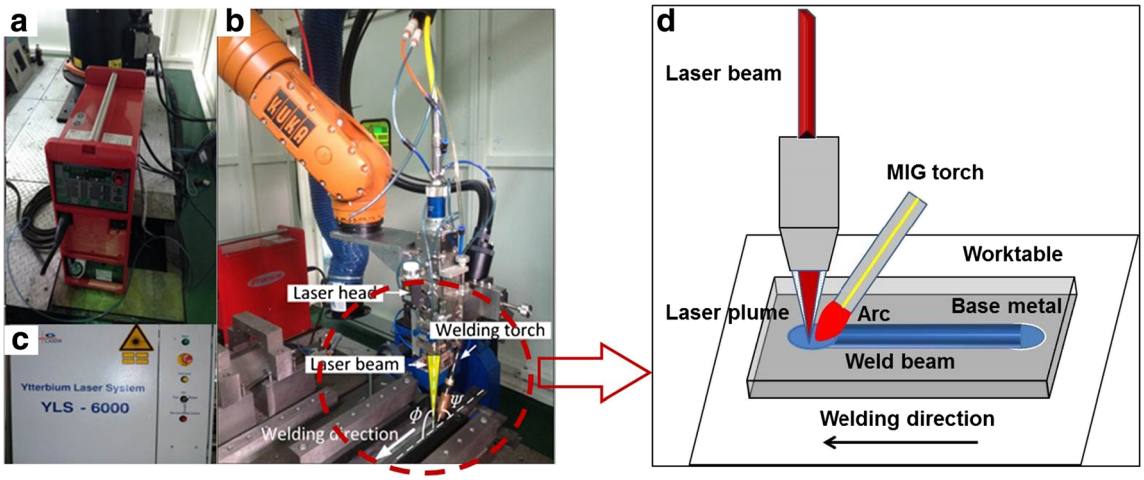

Fig. 1 The experimental setup. **a** TPS-5000 FRONIUS welding machine. **b** YLS-6000 fiber laser. **c** Kuka (KR30H) welding robot **d** Schematic drawing of laser–MIG hybrid welding

where $\lambda_{ij}(i, j = x, y, z)$ is the thermal conductivity tensor component along the x, y, and z directions, T is the location time-dependent temperature, ρ is the density of the material, c is the specific heat, t is the time, and Q is the heat generated in the control volume, which can be written as follows:

$$Q = q_{Laser}(x, y, z) + q_{MIG}(x, y, z) \tag{2}$$

where $q_{Laser}(x, y, z)$ is the laser heat input and $q_{MIG}(x, y, z)$ is the arc heat input.

To analyze heat transfer during the laser–MIG hybrid welding, there are two kinds of heat transfer modes, i.e., radiation and convection. The boundary heat transfer (from specimen to fixture) is too small to be considered, while the radiation must be taken into account since the high temperature during welding process. Furthermore, the initial temperature is assumed to be 25 °C.

The heat transfer modes can be expressed as follows:

$$q_0 = \varepsilon\sigma\left(T^4 - T_0^4\right) + \beta(T - T_0) \tag{3}$$

where T is the temperature of weldment, $T_0 = 25$ °C is the ambient temperature, ε is the emissivity, $\sigma = 0.5$ is the Stefan–Boltzmann constant, and $\beta = 40$ Wm^{-2} K^{-1} is the convective heat transfer coefficient.

3.3 Heat source model

Hybrid welding contains laser heat source and arc heat source; the former has a keyhole effect and the latter produces ellipsoid molten pool [15]. Therefore, it is not accurate to use single heat source to simulate the thermal loading during the laser–MIG hybrid welding process. A combined heat source model consisting of a double-ellipsoid heat source and a conical heat source is adopted to characterize the laser–MIG hybrid welding. In the current study, some parameters of the combined heat source model are validated or revised by experiment method. The schematic of the heat source model is shown in Fig. 3.

The double-ellipsoid heat source has two sections (i.e., front ellipsoid and rear ellipsoid), which are formulated as follows [15]:

$$q_1(x,y,z) = \begin{cases} q_r(x,y,z) = \dfrac{6\sqrt{3}f_r Q}{\pi^{2/3} a c_r h_1} \exp\left(-3\left(\left(\dfrac{x}{a}\right)^2 + \left(\dfrac{y}{h_1}\right)^2 + \left(\dfrac{z}{c_r}\right)^2\right)\right) & if\ z \in [-c_r, 0] \\ q_f(x,y,z) = \dfrac{6\sqrt{3}f_f Q}{\pi^{2/3} a c_f h_1} \exp\left(-3\left(\left(\dfrac{x}{a}\right)^2 + \left(\dfrac{y}{h_1}\right)^2 + \left(\dfrac{z}{c_f}\right)^2\right)\right) & if\ z \in [0, c_f] \end{cases} \tag{4}$$

where q_f and q_r are the weld flux rates per unit volume in the front and rear ellipsoids, respectively, h_1 is the depth of the double-ellipsoid heat source, a is the width of the

Table 1 Chemical composition of base material

Element	Ni	C	Si	Mn	P	S	Cr	Co	Fe
Invar alloy (base)	35.5–36.5	≤ 0.01	≤ 0.2	0.2–0.4	≤ 0.007	≤ 0.002	≤ 0.15	≤ 0.4	Based
Invar M93 (filler wire)	36.20	–	0.53	0.55	–	0.53	0.23	–	61.43

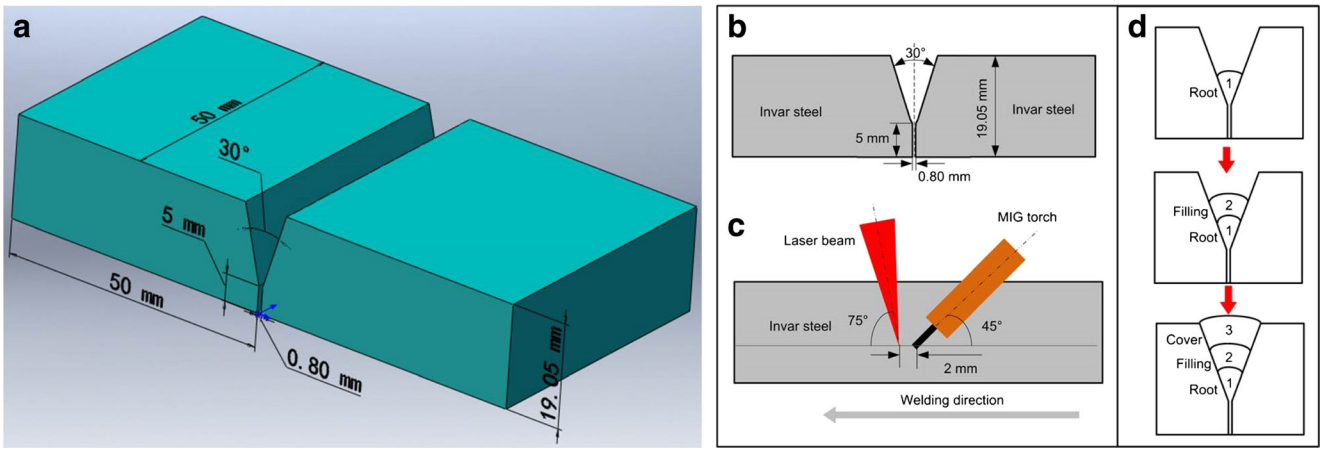

Fig. 2 Specimen structure and size

double-ellipsoid heat source, $Q = \eta VI$ is the applied power, η is the effective coefficient and $\eta = 0.8$, V is the Weld voltage, I is the weld current, c_f and c_r are the lengths of front ellipsoid and rear ellipsoid, and f_f and f_r are dimensionless factors given by

$$\begin{aligned} f_f &= \frac{2}{1 + c_r / c_f} \\ f_r &= \frac{2}{1 + c_f / c_r} \\ f_f + f_r &= 2 \end{aligned} \tag{5}$$

The conical heat source model is described as follows:

$$\begin{aligned} q_2(x,y,z) &= \frac{9Q_L}{\pi(1-e^{-3})} \cdot \frac{1}{(z_e - z_i)\left(r_e^2 + r_e r_i + r_i^2\right)} \cdot \exp\left(-\frac{3(x^2+z^2)}{r_c^2}\right) \\ r_c &= f(z) = r_i + (r_e - r_i)\frac{y - y_i}{y_e - y_i} \end{aligned} \tag{6}$$

where r_e means the maximum radius of the conical heat source, r_i means the minimum radius of the conical heat source, y_e is the maximum value along the y axis direction, y_i is the minimum value along the y axis direction, and Q_L is the effective power. The laser equipment can calculate the effective power.

Based on the Eqs. (4) and (6), the combined heat source model is defined by the following:

$$\begin{cases} q_{MIG}(x,y,z) = f_1 q_1(x,y,z) & if\ 0 \le y \le h_1 \\ q_{Laser}(x,y,z) = f_2 q_2(x,y,z) & if\ h_1 \le y \le h_1 + h_2 \end{cases} \tag{7}$$

where q_{MIG} and q_{Laser} are the MIG weld and laser weld flux rates per unit volume into the combined heat source, h_2 is the depth of the conical heat source, and f_1 and f_2 are the energy distribution factors and

$$\begin{aligned} f_1 &= \frac{V_1}{V_1 + V_2} \\ f_1 + f_2 &= 1 \end{aligned} \tag{8}$$

where V_1 is the volume of double-ellipsoid heat source and V_2 is the volume of conical heat source, given by the following:

$$\begin{aligned} V_1 &= \frac{1}{3}\pi\left(c_r + c_f\right)a h_1 \\ V_2 &= \frac{1}{3}\pi\left(r_e^2 + r_i^2 + r_i r_e\right)h_2 \end{aligned} \tag{9}$$

Accordingly, the energy distribution factor can be expressed as follows:

$$\begin{aligned} f_1 &= \frac{\left(c_r + c_f\right)a h_1}{\left(c_r + c_f\right)a h_1 + \left(r_e^2 + r_i^2 + r_i r_e\right)h_2} \\ f_2 &= \frac{\left(r_e^2 + r_i^2 + r_i r_e\right)h_2}{\left(c_r + c_f\right)a h_1 + \left(r_e^2 + r_i^2 + r_i r_e\right)h_2} \end{aligned} \tag{10}$$

Table 2 Equipment parameters of laser–arc hybrid welding

Parameter	Value (type)
Laser power	6 kW
Laser mode	CW
Modulation frequency	5 kHz
Starting current	8 A
Arc mode	Pulsed arc
Arc current	3–500 A
Arc voltage	3 × 400 V (± 15%, 50/60 Hz)
Power coefficient	0.99 (500 A)
Torch angle	60 ± 3°
Filler wire diameter (type)	1.2 mm (solid)

Table 3 Laser–MIG hybrid welding parameters

Sample No.	Weld layer	Laser power (W)	Weld current (*I*)	Weld voltage (V)	MIG power (W)	Ratio between laser and MIG power	Weld speed/ (m min^{-1})
No. 1	Root	5000	240	24.3	5832	1.17	1
	Filling	2200	250	24.6	6150	2.80	0.35
	Cover	2000	300	26.6	7980	3.99	0.35
No. 2	Root	5500	240	24.3	5832	1.06	1
	Filling	2400	250	24.6	6150	2.56	0.35
	Cover	2200	300	26.6	7980	3.63	0.35
No. 3	Root	6000	240	24.3	5832	0.97	1
	Filling	2600	250	24.6	6150	2.37	0.35
	Cover	2400	300	26.6	7980	3.33	0.35

3.4 Material properties

Material's physical and mechanical properties change with temperature. In order to obtain accurate simulation results, it is essential to use physical properties parameters at different temperatures. The material properties used in simulation are shown in Fig. 4. The three curves are obtained by [4] and interpolation, which are the specific heat, thermal conductivity, and density change with the temperature.

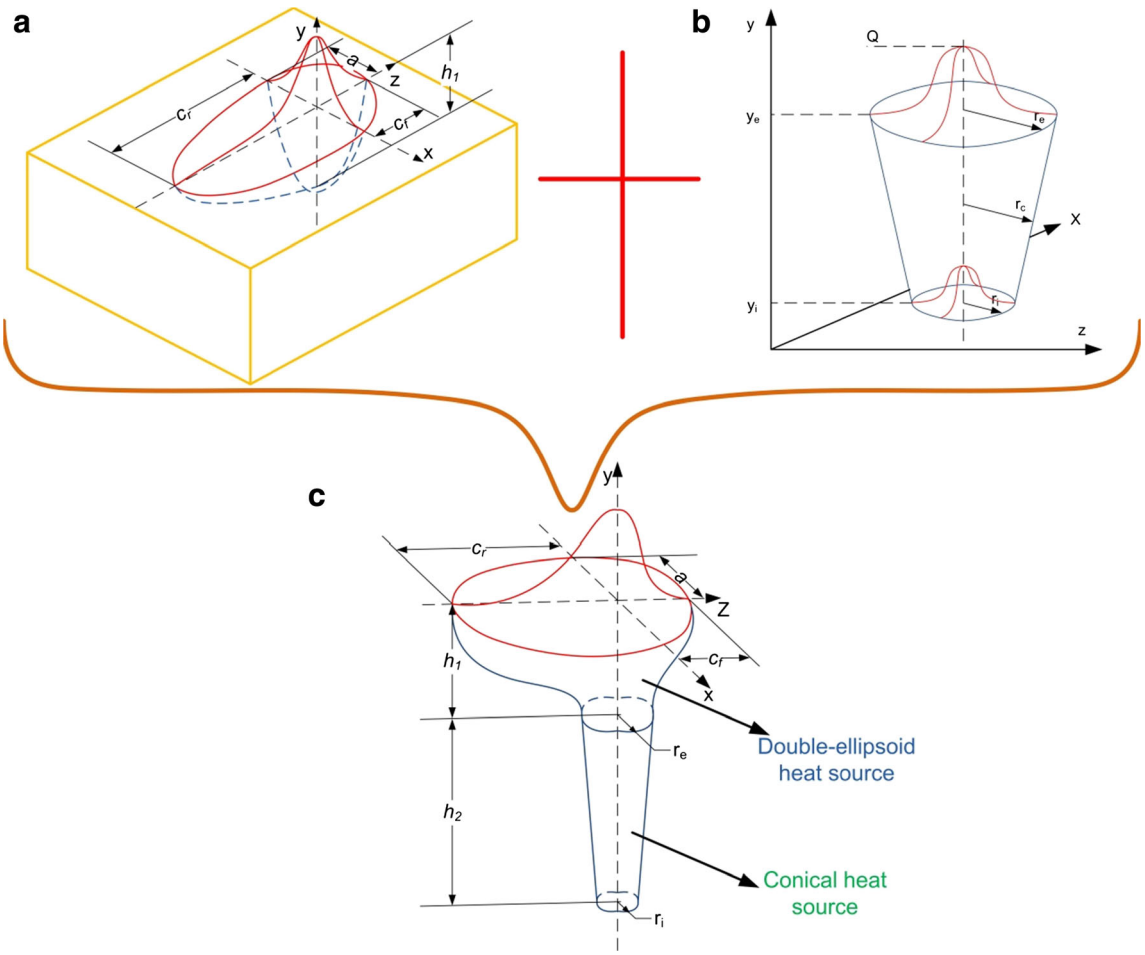

Fig. 3 Combined heat source model

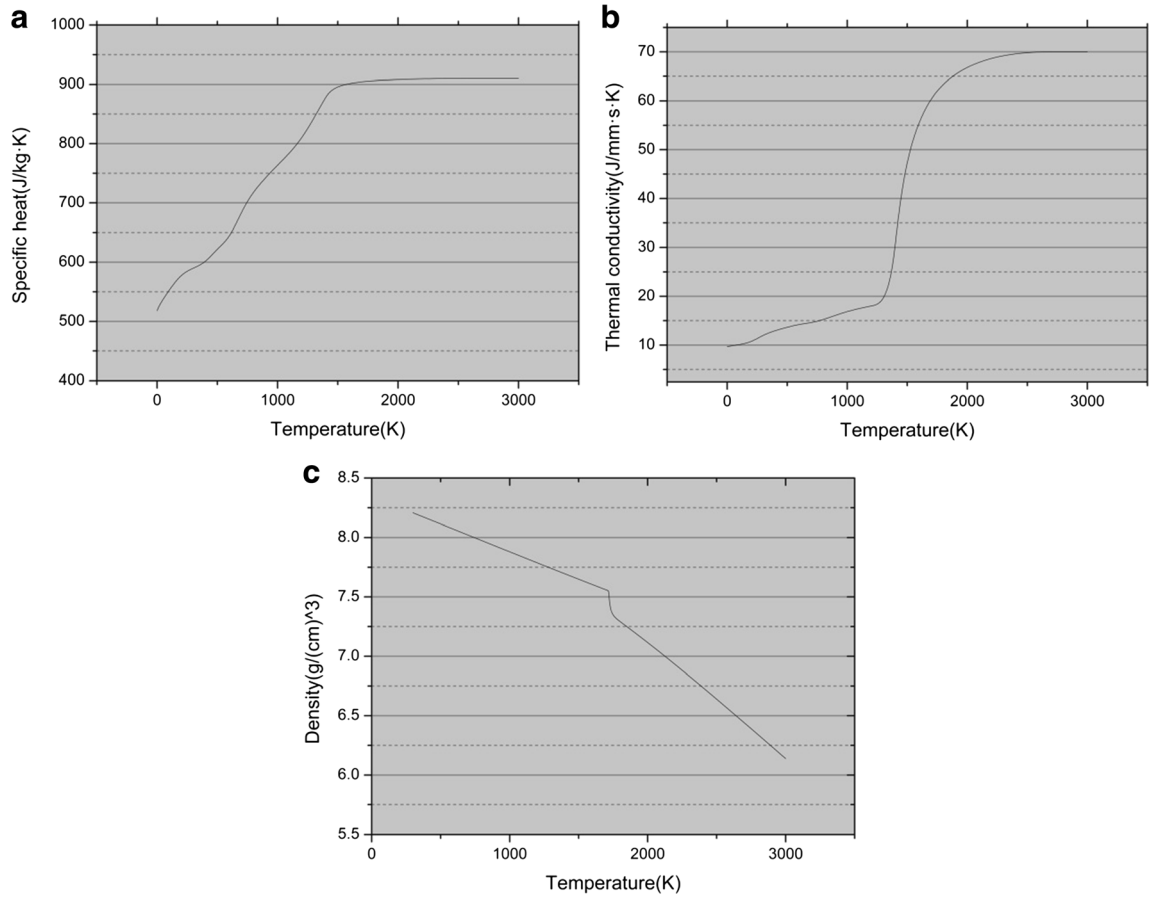

Fig. 4 Material properties with the change of temperature. **a** Specific heat. **b** Thermal conductivity. **c** Density

4 Results and discussion

4.1 Morphology

The macromorphology of laser–MIG hybrid welded joints is shown in Fig. 5, where the macrotopography parameters are extracted.

Figure 5 shows that the weld joint is penetrated fully, and the adjacent layer is fused well. In order to estimate if the welded joint is good or not in shape, the weld size of different layers is measured (Fig. 8a, b). It can be seen that the weld width grows gradually from root weld to cover weld, but the weld depth declines, with the transformation of the weld shape from goblet to nail, which means that the heat source model above is reasonable. Due to the rather low welding speeds used here (typically less than 5 m min^{-1}), the cross section of a weld with the laser alone shows the well-known nail head shape or goblet head shape, and the surface melt pool shows the characteristic humps observed round the keyhole rim for these welding conditions. The MIG cross section shows the characteristic height seam reinforcement, with a penetration depth that is much lower than in a laser case.

Consequently, the full penetration is achieved more easily with increasing ratio of energy distribution factor. However, according to Fig. 5, it is not possible to distinguish how much penetration varies with increasing ratio of energy distribution factor due to a fair approximation of penetration for same class of layer in all cases. For the hybrid process, one can observe a greater keyhole penetration compared to the laser alone and the geometry of the reinforcement similar to the one obtained with the MIG process alone.

Considering the quality, it is noticeable that all weld centerlines have rotation, due to different ratios of energy distribution. Figure 5d–f shows that the weld centerline rotates clockwise as the ratio of energy distribution increases. The rotating problem can be also related to electromagnetic force generated by the interaction between the self-induced magnetic field and welding current flowing through the workpiece. The role of electromagnetic force generated is that the plasma flow induced in keyhole by laser and arc direction is changed. The electromagnetic force can be expressed as follows [26, 27]:

$$\overrightarrow{F} = \overrightarrow{J} \times \overrightarrow{B} = B_\theta \left(J_z \overrightarrow{z} - J_r \overrightarrow{r} \right) \tag{11}$$

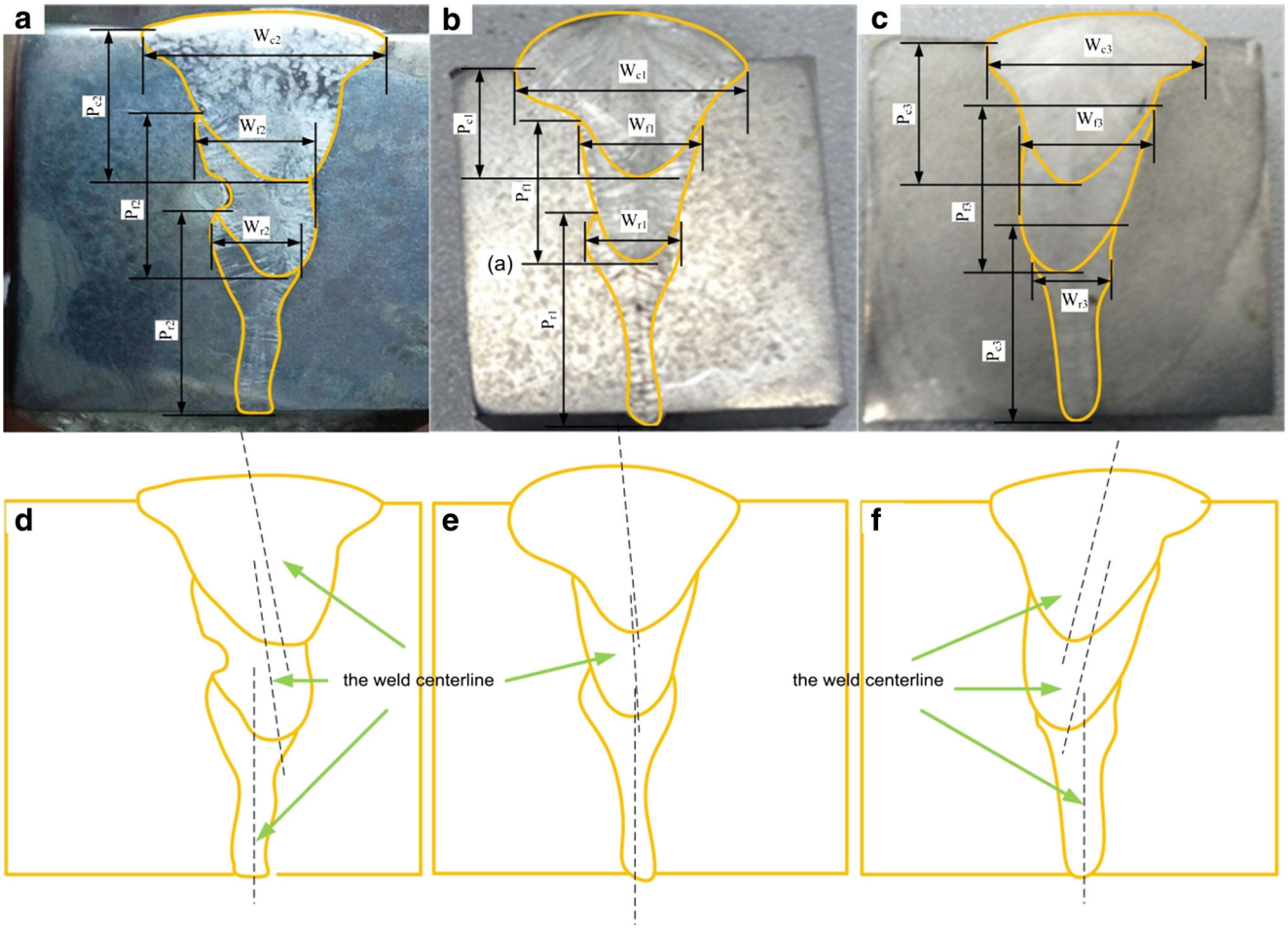

Fig. 5 Macrotopography parameters of Invar alloy weld with different process parameters. **a** Test positions of specimen No. 1. **b** Test positions of specimen No. 2. **c** Test positions of specimen No. 3. **d** The weld centerline positions of specimen No. 1. **e** The weld centerline positions of specimen No. 2. **f** The weld centerline positions of specimen No. 3

where

$\vec{J}$ = plasma flow density vector

$\vec{B}$ = magnetic flux vector

B_θ = magnetic permeability

In Eq. (11), the magnetic permeability is positively related to welding current and the plasma flow density is positively related to plasma concentration. Thus, as for fixed weld current, increasing laser power with increment of ratio of energy distribution induces more plasma concentration.

When the ratio of energy distribution decreases, arc power increases with respect to laser power, increasing the welding current. Thus, the increment of electromagnetic force results in the greater rotation, of which schematic drawing is shown in Fig. 6. Essentially, it can be found that the increment of electromagnetic force tips the dynamic balance between keyhole and melt pool.

4.2 The simulation results

In order to analyze these experimental observations by using simulations, the commercial finite element software package MSC Marc is used to perform the simulation for the hybrid welding. The filling element heat source is loaded by weld filler as well as the combined heat source is loaded into the software by a subroutine named as "uweldflux.f." The finite element equations are constructed and solved by MSC Marc. The cross sections of weld beam simulated at 0.5 s are shown in Fig. 7, when the hybrid welding process is stable. The white area is the fusion zone, which is over 1500 °C more than the melting point of Invar alloy, and the simulation results are similar to the experimental results. The weld centerline has no rotation because the electromagnetic force model is not added during hybrid welding.

It can be found that the molten pool shape is different due to the difference of ratios of energy distribution factor in Fig. 7. Despite that laser power is maintained and MIG power becomes higher, the heat input decreases when the ratio of energy distribution factor decreases from 1.17 to 0.97. Also, the welding mode has a transition from heat conduction welding to deep penetration welding. For laser power decreases with respect to MIG power when the ratio of energy distribution factor decreases, the amount of evaporation is

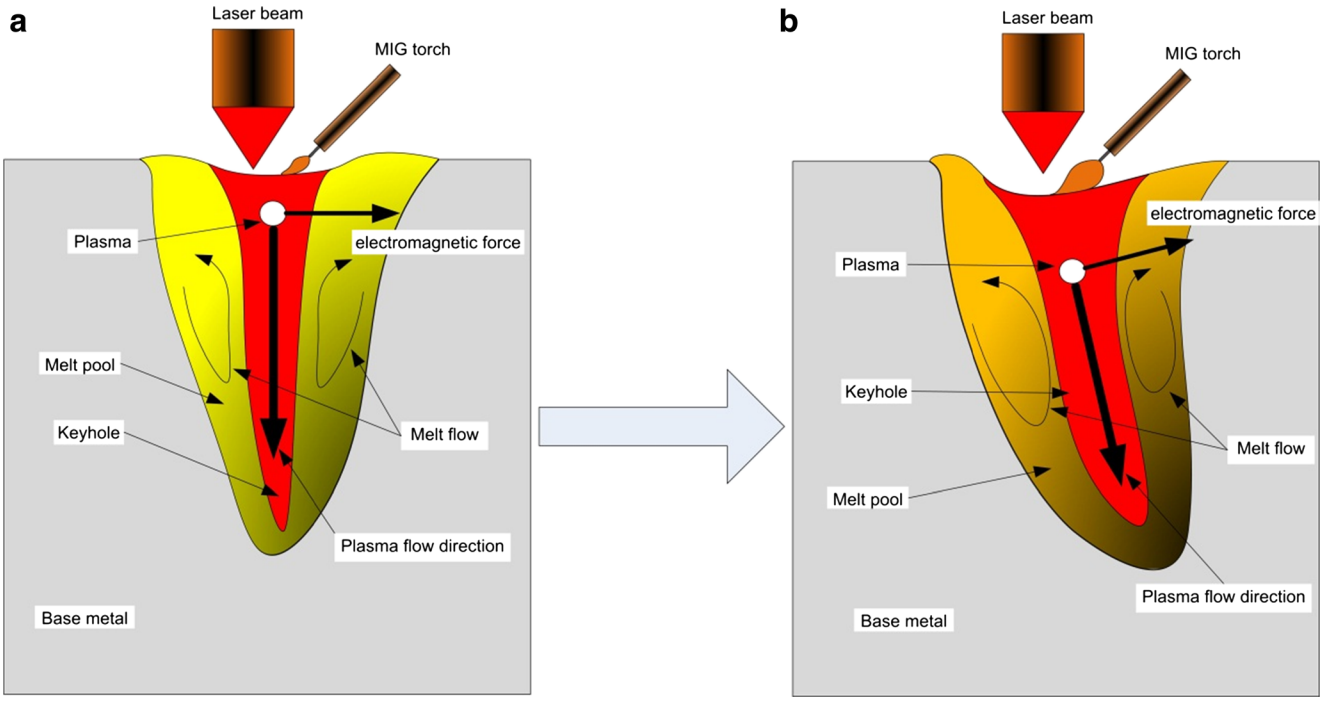

Fig. 6 The action of electromagnetic force on plasma. **a** Before the plasma flow direction changes. **b** After the plasma flow direction changes

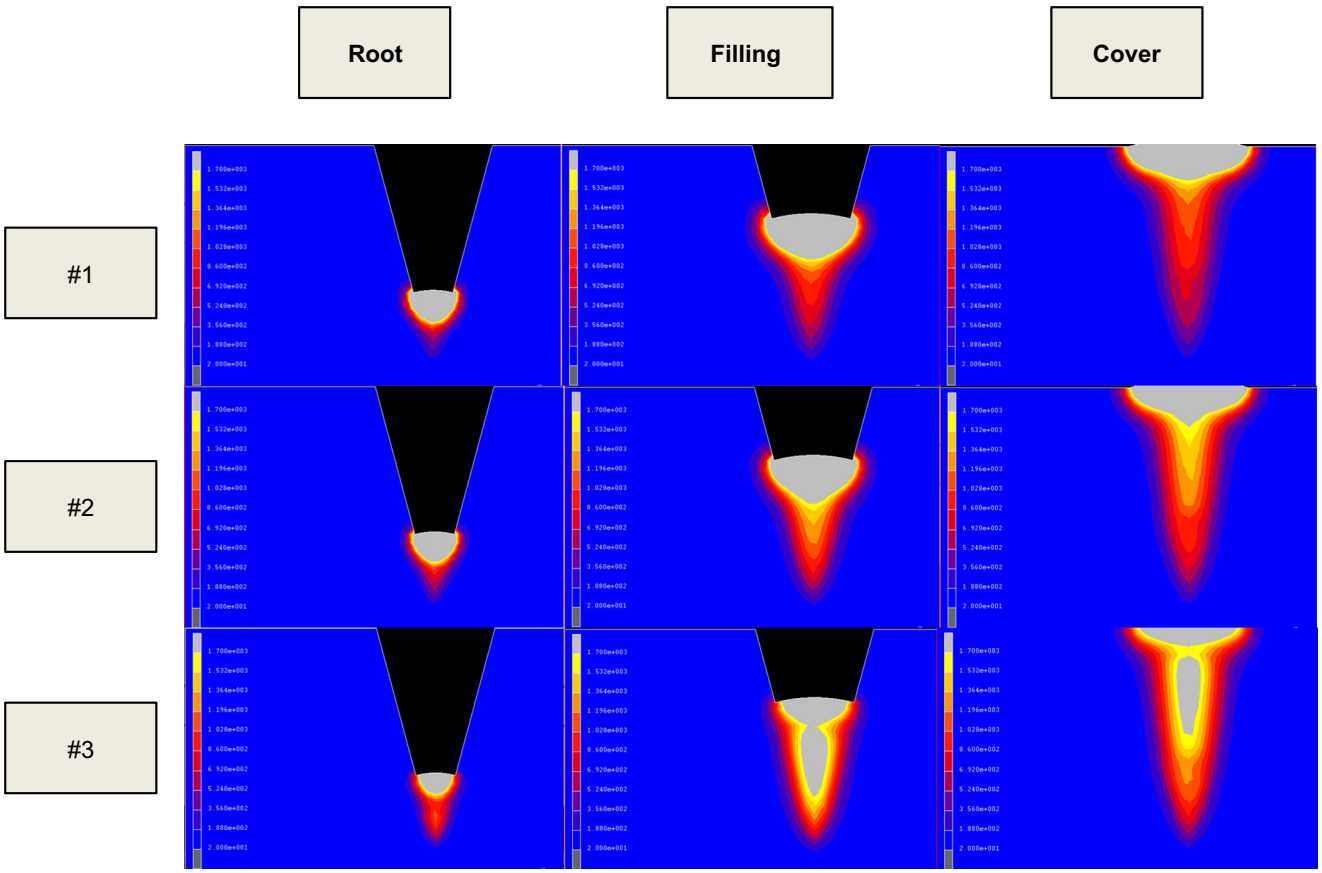

Fig. 7 The cross sections of weld beam calculated at 0.5 s with different welding parameters

relatively small and the effect of current concentration decreases. Consequently, the local increase of plasma temperature gradually disappears. On the contrary, the local increase of plasma temperature in the vicinity of laser irradiation is extended and the absolute value of temperature also increases when the laser power is higher with respect to MIG power.

When the laser and arc plasma are used simultaneously, each heat source mutually assists and influences the other. The generation of intensive metal vapor over the laser-irradiated position improves the characteristics of hybrid plasma. When the laser is irradiated on the metal surface, sufficient energy of light can cause metal vaporization and metal vapor can be further developed to LIP (laser-induced plasma) plume by continuous supply of more laser energy. Because LIP is generated inside the arc plasma in laser–arc hybrid welding, two kinds of plasma interact and affect each other. The specimen No. 3 in Fig. 7 shows that specimen interior is heated to melt by laser beam through arc melting zone more deeply with reducing ratio of energy distribution factor. Thus, the arc plasma concentrates into the top of keyhole, and LIP concentrates into the bottom of the keyhole. In addition, the neck can be seen clearly due to the interaction between the arc plasma and LIP.

4.3 Comparative study between experimental and simulated results

Thermal characteristics have been observed through three-dimensional heat conduction analysis for hybrid welding. Nine groups of simulation are designed to investigate the influence of ratios of energy distribution factor for molten pool shape quantitatively, and the comparison for the simulation results and the experimental results are shown in Fig. 8.

According to Table 3, the ratio of energy distribution factor decreases from specimen No. 1 to specimen No. 3 and from cover welding to root welding. It can be concluded that the simulation is in agreement with experimental results by comparing Fig. 8a, b to c, d. As the ratio of energy distribution factor changes, the weld width of root weld and filling weld is closer. However, the weld width of cover weld has difference with root weld and filling weld. As for weld penetration, there is difference among all layers. In these cases, it is possible that the groove type and the ratio of energy distribution factor are the main effecting factors in weld width of each layer, but the ratio of energy distribution factor is the main effecting factors in weld penetration of each layer, particularly laser power.

Also, Fig. 8 shows that weld penetration and weld width increase with the increase of laser power from 5 to 6 kW, whereas the former has more obvious indication, because the effect of laser heat source is more significant than MIG heat source; with the increase of arc power from 5.832 to 7.98 kW, the effect of arc heat source is more significant, increasing the weld penetration, meanwhile weld width and having better weld width. Furthermore, as the ratio of energy distribution factor (f_1/f_2) is changed, the weld width and weld penetration are changed. The ratio has greater value and the effect of arc heat source is more significant; otherwise, the effect of laser heat source is more significant.

Weld width increasing with decreasing ratio of energy distribution factor is due to the MIG power contribution. For higher MIG power, a higher portion of base metal in the outlet keyhole fuses under the action of the electric arc, which increased weld width. At fixed MIG power, the weld width is lower for the samples processed at higher laser power because of the stabilization effect induced on MIG arc by higher laser power. As MIG power increased, the arc force possibly started to work at the outlet of the keyhole instead of acting at the inner of the keyhole, which rises weld penetration. As discussed above, the MIG arc is more stable at the highest laser power when metal vaporization is favored. Metal vaporization, leading to higher vapor pressure, pushed the melt towards the joint bottom causing the expulsion of the molten metal and a metal vacancy at the joint top.

4.4 Microstructure

In order to analyze the difference of temperature field of different layers quantificationally, with aided analysis of microstructure, the thermal cycle curves at different locations (nodes 1, 2, and 3) for the three components are shown in Fig. 9.

The three nodes are located in weld seam, next to different layers, respectively. It is apparent that the heat source goes through the place during the welding, where temperature is abruptly changing with temperature excursion. The heat input increases constantly from root welding to cover welding, regardless of the accumulation of heat in workpieces. Thus, it can be concluded that the last welding can preheat the next welding, and the next welding can temper the last welding.

Figure 9 shows that the accumulation of heat is obvious during the multi-layer laser–MIG hybrid welding. The heat accumulated leads to grain remelting partly and overgrowth of grain partly. In addition, the heat accumulated is most serious in cover welding process, and coarser columnar can be found in cover welding as shown in Fig. 10i. Consequently, it is necessary that an appropriate cooling time is conformed. During the welding, the temperature field influences grain size and growth. The microscopic structure of each weld layer is shown in Fig. 10.

Equiaxed grains are dominant in the weld centerline while closure to the fusion zone (FZ)/base metal (BM) interface directional columnar solidification structure is observed from the fusion boundary down to the certain depth of FZ (Fig. 10d, f, g). The thickness of the fine grain zone and its grain size do not change appreciably with ratio of energy

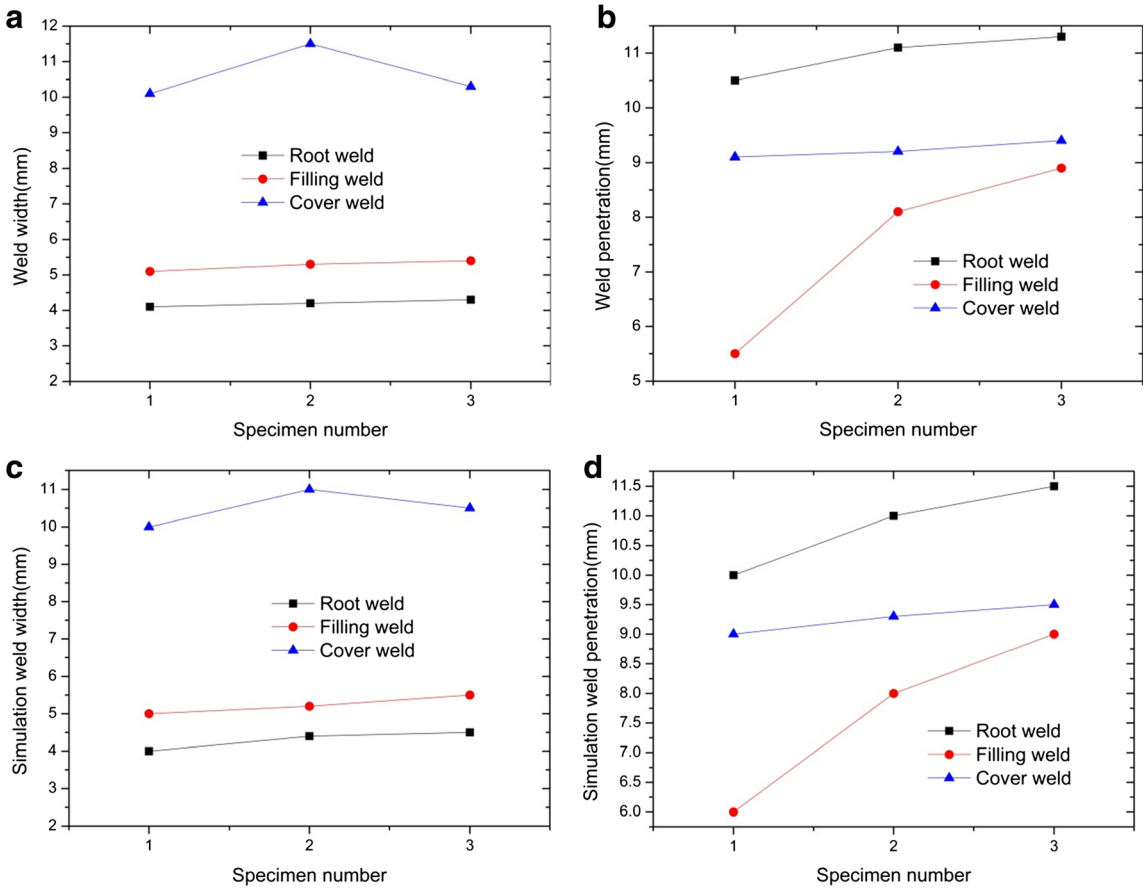

Fig. 8 The comparison for the simulation results and the experimental results. **a** Weld width. **b** Weld penetration. **c** Simulation weld width. **d** Simulation weld penetration

distribution factor. Weld microstructure is due to constitutional undercooling in the melt. When little undercooling occurs (as at the interface between FZ and BM), epitaxial growth develops from many nuclei with the same lattice structure of the BM grains (Fig. 10d, f). As undercooling increased, the formation of stable protrusions or dendrites occurs into the melt zone leading to the formation of columnar grains (Fig. 10d). Moving towards the weld centerline, both the shallow thermal gradient and the increased fluid flow lead to the transition from columnar to equiaxial growth (Fig. 10e).

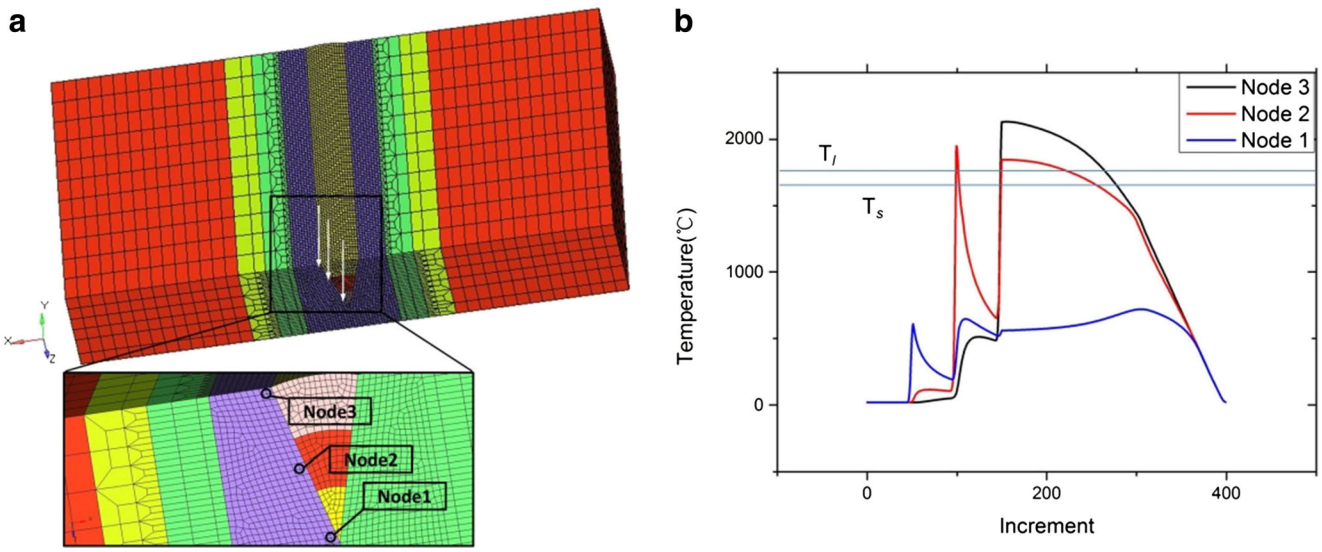

Fig. 9 The thermal cycle curves. **a** The position of three nodes. **b** The thermal cycle curves of three nodes

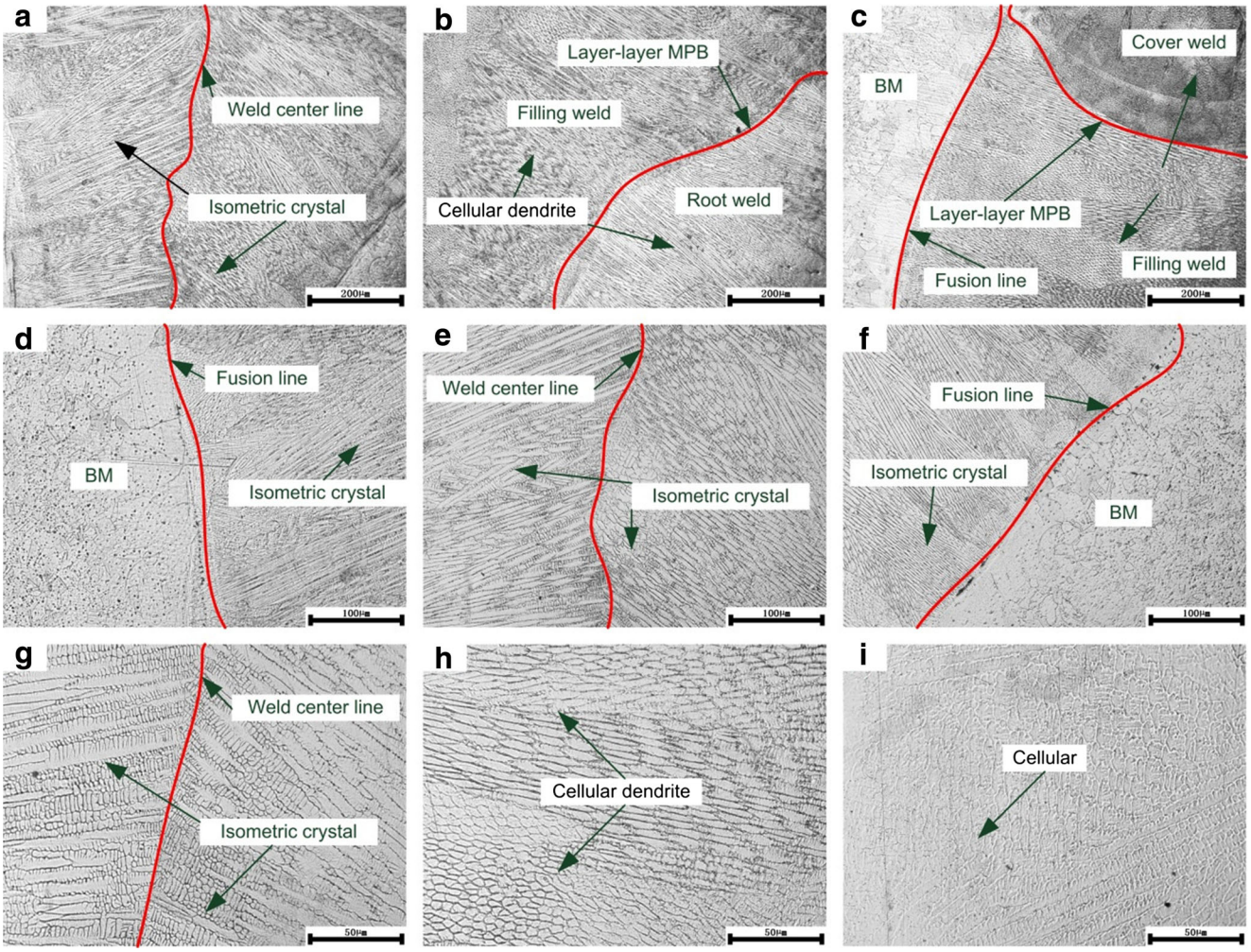

Fig. 10 Microscopic structure at weld seam center of each weld layer. **a** Root weld. **b** Root weld to filling weld. **c** Filling weld to cover weld. **d**–**f** Local of root weld. **g** The middle of root weld. **h** Filling weld. **i** Cover weld

Figure 10 clearly shows that the grain size of welding seam increases from root welding to cover welding, with the transition from columnar dendrites to cellular dendrites and cellular crystal due to the increasing heat input and the accumulation of heat which promotes grain growth. It can be seen that there is a weld centerline in Fig. 10a root welding, of which the grain coarsens with the distance from the weld centerline, because of heat treatment of the next welding. On the hand, the more obvious synergy of arc and laser and the lower weld speed from root weld to cover weld improve heat input; on the other hand, the bigger volume of weld pool and reducing solidification rate make the grain grow fully. Thus, it is obvious that the grain size in cover weld is coarser than in root weld (Fig. 10b, c).

From Fig. 10d, f, it is obvious that the grain size in weld seam is coarser than that in base metal as the studied material has low thermal conductivity. Thus, the difference in heat dissipation capacity leads to grain coarsening of austenite in the weld area. The ratio shows a smaller value, and isometric grain can be formed more easily (Fig. 10a, e, g). Because the weld metal is heated by the laser heat source more than the arc heat source and solidifies rapidly, isometric grain can be found in root weld and filling weld. Thus, ratios of energy distribution factor (f_1/f_2) affect grain type; heat input affects grain size.

5 Conclusions

In the present study, the results may be summarized as follows:

1. According to the macromorphology of laser–MIG hybrid welded joints, a combined heat source consisting of a double-ellipsoid heat source and a conical heat source is proposed. Furthermore, the energy distribution factor is produced.
2. Laser–MIG welding experiments are carried out to verify the combined heat source. The simulated results are found in good agreement with the experimental results, which illustrates that it is an entirely feasible method to use FEM

to simulate the shape of molten pool under different energy distribution factors for laser–MIG hybrid weld. Moreover, the method can assist process design and optimization in terms of productivity and operational costs.

3. The weld shape transfers from the goblet into the nail from root welding to cover welding. The thermal cycle curves indicate that the smaller effect of laser and the bigger effect of arc cause the increasing weld width and the declining weld depth. In other word, the increasing ratio of laser energy in hybrid welding can increase the weld penetration depth and the increasing ratio of arc energy in hybrid welding can increase the weld width.
4. The grain size in hybrid weld shows that the ratio of laser energy and arc energy from root welding to cover welding is changing. It is noted that it is necessary for every layer to cool weld joint appropriately during the continuous multi-layer laser–MIG hybrid welding, due to the increasing heat input and the accumulation of heat which promotes grain growth.
5. The electromagnetic force generated by the interaction between the self-induced magnetic field and welding current flowing through the workpiece results in weld centerline rotation. The role of electromagnetic force generated is that the plasma flow induced in keyhole by laser and arc direction is changed. When the ratio of energy distribution decreases, arc power increases with respect to laser power, resulting in the greater rotation for centerline rotation.

Acknowledgements The authors gratefully acknowledge the financial support of the National Commercial Aircraft Manufacturing Engineering Technology Research Center Innovation Fund of China (SAMC14-JS-15-057) and a project funded by Shanghai Municipal Commission of Economy and Informatization (15-XI-1-15).

References

1. Kakehashi Y (1981) Theory of the Invar effect in FeNi alloy. J Phys Soc Jpn 50(7):2236–2245
2. Zhan X, Liu J, Chen J, Peng Q, Wei Y, Zhao Y (2016) Parameter optimization of multi-pass multi-layer MIG welded joint for invar alloy. The Int J Adv Manuf Tech 87(1–4):601–613
3. Corbacho JL, Suárez JC, Molleda F (1998) Welding of invar Fe-36Ni alloy for tooling of composite materials. Weld Int 12(12):966–971
4. Xu PQ, Ren JW, Zhang PL, Gong HY, Yang SL (2013) Analysis of formation and interfacial WC dissolution behavior of WC-Co/invar laser-TIG welded joints. J Mater Eng Perform 22(2):613–623
5. Xu PQ, Bao CM, Lu FG, Ma CW, He JP, Cui HC, Yang SL (2011) Numerical simulation of laser–tungsten inert arc deep penetration welding between WC–Co cemented carbide and invar alloys. Int J Adv Manuf Tech 53(9–12):1049–1062
6. Zhan X, Li Y, Ou W, Yu F, Chen J, Wei Y (2016) Comparison between hybrid laser-MIG welding and MIG welding for the invar36 alloy. Opt Laser Technol 85:75–84
7. Zain-Ul-Abdein M, Nelias D, Jullien JF, Deloison D (2008) Thermo-mechanical analysis of laser beam welding of thin plate with complex boundary conditions. Int J Mater Form 1(1):1063–1066
8. Wang Q, Chen H, Zhu Z, Qiu P, Cui Y (2016) A characterization of microstructure and mechanical properties of A6N01S-T5 aluminum alloy hybrid fiber laser-MIG welded joint. Int J Adv Manuf Tech 86(5–8):1375–1384
9. Tani G, Campana G, Fortunato A, Ascari A (2007) The influence of shielding gas in hybrid LASER–MIG welding. Appl Surf Sci 253(19):8050–8053
10. Ghosal S, Chaki S (2010) Estimation and optimization of depth of penetration in hybrid CO 2 LASER-MIG welding using ANN-optimization hybrid model. Int J Adv Manuf Tech 47(9):1149–1157
11. Faraji AH, Goodarzi M, Seyedein SH, Barbieri G, Maletta C (2015) Numerical modeling of heat transfer and fluid flow in hybrid laser–TIG welding of aluminum alloy AA6082. Int J Adv Manuf Tech 77(9–12):2067–2082
12. Campana G, Fortunato A, Ascari A, Tani G, Tomesani L (2007) The influence of arc transfer mode in hybrid laser-MIG welding. J Mater Process Tech 191(1):111–113
13. Gao Z, Wu Y, Huang J (2009) Analysis of weld pool dynamic during stationary laser–MIG hybrid welding. Int J Adv Manuf Tech 44(9–10):870–879
14. Hong H, Han Y, Du M, Tong J (2016) Investigation on droplet momentum in VPPA-GMAW hybrid welding of aluminum alloys. Int J Adv Manuf Tech 86(5–8):2301–2308
15. Guoxiang X, Chuansong W, Guoliang Q, Xuyou W, Shangyang L (2008) Numerical simulation of weld formation in laser plus GMAW hybrid welding. Acta Metall Sin 44(6):641–646
16. Chen YB, Lei ZL, Li LQ, Wu L (2006) Experimental study on welding characteristics of CO2 laser TIG hybrid welding process. Sci Technol Weld Joi 11(4):403–411
17. Hu B, Richardson IM (2006) Mechanism and possible solution for transverse solidification cracking in laser welding of high strength aluminium alloys. Mater Sci Eng A 429(1):287–294
18. Kong F, Ma J, Kovacevic R (2011) Numerical and experimental study of thermally induced residual stress in the hybrid laser-GMA welding process. J Mater Process Tech 211(6):1102–1111
19. Zhan X, Liu Y, Ou W, Gu C, Wei Y (2015) The numerical and experimental investigation of the multi-layer laser-MIG hybrid welding for Fe36Ni Invar alloy. J Mater Eng Perform 24(12):4948–4957
20. Bidi L, Mattei S, Cicala E, Andrzejewski H, Le Masson P, Schroeder J (2011) The use of exploratory experimental designs combined with thermal numerical modelling to obtain a predictive tool for hybrid laser/MIG welding and coating processes. Opt Laser Technol 43(3):537–545
21. Piekarska W, Kubiak M (2011) Three-dimensional model for numerical analysis of thermal phenomena in laser–arc hybrid welding process. Int J Heat Mass Tran 54(23):4966–4974
22. Xu GX, Wu CS, Qin GL, Wang XY, Lin SY (2011) Adaptive volumetric heat source models for laser beam and laser + pulsed GMAW hybrid welding processes. Int J Adv Manuf Tech 57(1–4):245–255
23. Le Guen E, Carin M, Fabbro R, Coste F, Le Masson P (2011) 3D heat transfer model of hybrid laser Nd: Yag-MAG welding of S355 steel and experimental validation. Int J Heat Mass Tran 54(7):1313–1322
24. Leo P, Renna G, Casalino G, Olabi AG (2015) Effect of power distribution on the weld quality during hybrid laser welding of an Al-Mg alloy. Opt Laser Technol 73:118–126
25. Kim YC, Hirohata M, Murakami M, Inose K (2015) Effects of heat input ratio of laser–arc hybrid welding on welding distortion and residual stress. Weld Int 29(4):245–253
26. Goldak J, Chakravarti A, Bibby M (1984) A new finite element model for welding heat sources. Metall Trans B 15(2):299–305
27. Kou S, Sun DK (1985) Fluid flow and weld penetration in stationary arc welds. Metall Trans A 16(2):203–213